Available online at www.sciencedirect.com
ScienceDirect
Polymer 48 (2007) 3749–3758
polymer
www.elsevier.com/locate/polymer

Reaction-induced phase decomposition of thermoset/thermoplastic blends investigated by energy filtering transmission electron microscopy

Yonggui Liao [a], Shin Horiuchi [a,*], Jun Nunoshige [b], Haruo Akahoshi [c], Mitsuru Ueda [d]

[a] *Nanotechnology Research Institute, National Institute of Advanced Industrial Science and Technology (AIST), 1-1-1 Higashi, Tsukuba, Ibaraki 305-8565, Japan*
[b] *Japan Chemical Innovation Institute (JCII), O-okayama 2-12-1, Meguro-ku, Tokyo 152-8552, Japan*
[c] *Materials Research Laboratory, Hitachi Ltd., 1-1-7 Omika, Hitachi, Ibaraki 319-1292, Japan*
[d] *Department of Organic and Polymeric Materials, Tokyo Institute of Technology, 2-12-1 O-okayama, Meguro-ku, Tokyo 152-8552, Japan*

Received 10 January 2007; received in revised form 12 April 2007; accepted 21 April 2007
Available online 4 May 2007

Abstract

Energy-filtering transmission electron microscopy (EFTEM) was employed to investigate the morphology developments of thermoset/thermoplastic blends of poly(2,6-dimethyl-1,4-phenylene ether)/bis(vinylphenyl) ethane, PPE/BVPE. Neither conventional TEM images nor energy-filtered images at any energy loss levels showed any evidences for the phase separation of the blends, while those could be shown and characterized by the oxygen maps representing the differences in the oxygen concentrations between the two phases, which could be characterized as the PPE-rich phase (oxygen-rich phase) and the BVPE-rich phase (oxygen-poor phase). The blends undergo phase decomposition into the two phases through the crosslinking reaction of BVPE. The effect of the composition and the curing time on the phase decomposition behaviors was investigated by quantitative analysis of EELS spectra acquired from the two phases. Reactive functional moiety was introduced onto PPE and the effect of the reaction between the two components on the phase decomposition behaviors was also investigated. We show the possibility of EFTEM for the investigation of the mechanism of reaction-induced phase separations.

Keywords: Reaction-induced phase decomposition; EFTEM; Elemental map

1. Introduction

A growing fraction of plastics produced and used at present are multi-component polymer systems. Blending of two or more polymers permits optimization of properties that are often unobtainable or less economical than in any single homopolymer or copolymer. Immiscible blends can often give properties that exceed either of its components. Those synergistic effects achieved by fusion of different polymer materials are generated on the basis of multi-phase structures formed as a result of the interactions between the components and of processing conditions. Therefore, the characterization of morphologies and their development processes are of quite importance for the development of new polymeric materials by combining commercial polymers.

Reaction-induced phase decomposition has been known as one of the morphology development process of the multi-component polymer systems, where a blend of a polymer and a monomer undergoes a phase separation with increase of the molecular weight during the polymerization of the monomer [1–11]. Due to the complexity caused by the competitions between the polymerization and phase separation, many peculiar morphologies and structures, which is difficult to obtain by melt blending of polymers, such as sponge-like morphology [3], concentric/target patterns [4,5], labyrinthine patterns [4,6], plate-like crystals [7], chemically reactive physical gels [8], can be obtained.

* Corresponding author. Tel.: +81 29 861 6281; fax: +81 29 861 4437.
E-mail address: s.horiuchi@aist.go.jp (S. Horiuchi).

0032-3861/$ - see front matter © 2007 Elsevier Ltd. All rights reserved.
doi:10.1016/j.polymer.2007.04.054

Reaction-induced phase decomposition has been studied by employing mainly light scattering. On the other hand, obtained morphological variations can be studied by transmission electron microscopy (TEM) or scanning electron microscopy (SEM). TEM can provide much more detailed information on morphological features than SEM. However, conventional TEM necessitates heavy metal staining of specimens with OsO_4 or RuO_4 to produce sufficient elastically scattered electrons to give enough image contrast. The staining loses the chemical information that the components originally have and thus makes it difficult to explore further detailed features of phase separation processes [12]. Energy-filtering transmission electron microscopy (EFTEM), on the other hand, enables us to image polymer nanostructures without staining by electron spectroscopic imaging (ESI) and to perform quantitative chemical characterization of multi-phase structures by electron energy loss spectroscopy (EELS) [12–27]. EFTEM has a great potential to provide deep insights into multi-phase structures of polymer materials than conventional TEM, but there has been less works due to the difficulty of polymer specimens arising from the radiation sensitivity against electron beam.

In this work, we first time apply EFTEM to characterize the reaction-induced phase decomposition combining elemental mapping and EELS. Samples studied here are the blends of poly(2,6-dimethyl-1,4-phenylene ether) (PPE) and 1,2-bis-(vinylphenyl) ethane (BVPE). PPE is an attractive material in the electronics industry due to its low dielectric constant (2.45), a low dissipation factor (0.0007), and high glass transition temperature (T_g) of 210 °C. BVPE is a styrene-type crosslinker that can be cured at relatively low temperatures without a curing agent, and also possesses good thermal durability and dielectric properties (dielectric constant of 2.50 and dissipation factor of 0.0012) [28]. The blends of the two components are expected to provide materials with excellent dielectric properties, while overcoming the drawbacks of the two components: The brittle nature of the cured product of BVPE could be improved by blending of PPE, while the poor processability of PPE due to its high viscosity could be improved. The use of a thermoset resin as a ''reactive solvent'' in order to reduce the viscosity would be more friendly to the environment and more efficient than common organic solvents since the solvent removal is not required [29,30]. For that purpose, digycidyl ether of bisphenol A epoxy has been used for the reactive solvent for PPE. However, the good dielectric properties of PPE could not be maintained.

The morphology development of the PPE/BVPE blends through the crosslinking of BVPE is investigated by creating oxygen maps and by quantitative EELS analysis. The effect of the composition and the curing time on the phase decomposition behaviors was investigated by the intensity ratios of the oxygen K-ionization edges in EELS spectra acquired from the two phases. A reactive moiety was introduced onto PPE and the effect of the reaction between the two components on the phase decomposition behaviors was also investigated.

2. Experimental section

2.1. Materials

The chemical structures of the polymers used in this study, poly(2-allyl-6-methylphenol-*co*-2,6-dimethylphenol), allyl-PPE, and BVPE are shown in Scheme 1. 2,6-Dimethylphenol (DMP) was purified by recrystallization from *n*-hexane. 2-Allyl-6-methylphenol (AMP), PPE ($M_n = 17{,}000$, $M_w = 3.2$), copper chloride (I) (CuCl (I)) were purchased from Sigma-Aldrich Co., and vinylbenzyl chloride (70% *m*-isomer and 30% *p*-isomer) (VBC) was purchased from Tokyo Chemical Industrials Co., Japan. Dehydrated toluene, pyridine, tetrahydrofuran were purchased from Wako Pure Chemical Industries, Co., Japan. Other solvents and reagents were used as-received.

2.1.1. Synthesis of poly(2-allyl-6-methylphenol-co-2,6-dimethylphenol) (allyl-PPE)

Allyl-PPEs with AMP fraction ranging from 5 to 25 mol% were synthesized by the reported method [31,32]. A two-necked flask equipped with an oxygen inlet tube and a septum cap was charged with copper (I) chloride (0.04 g, 0.4 mmol), magnesium sulfate (6.0 g, 49.8 mmol), dry pyridine (100 ml 1.2 mol), and dry toluene (100 ml). The mixture was stirred at 25 °C under a stream of oxygen (50 ml/min), yielding a deep-green copper-pyridine complex catalytic solution. To this solution, A 50 ml toluene solution of 30 mmol of the two monomers (DMP and AMP) at various ratios was added. The mixture was stirred for 90 min under a stream of oxygen (50 ml/min), and then poured into methanol (1000 ml) containing concentrated 10 M HCl (5 ml). The precipitate was washed with methanol in several times, dissolved in chloroform, and, finally, reprecipitated into MeOH/HCl solution. After washing with methanol and drying at 80 °C for 3 h and 110 °C for 6 h under vacuum, a white fibrous polymer was obtained (yield: 3.37 g, 91%, $M_n = 24{,}000$, $M_w/M_n = 2.4$). The fraction of AMP in allyl-PPE was estimated from NMR spectra.

IR (KBr, ν, cm^{-1}): 1192 (Ar–O–Ar), 914 and 990 (C=C). ^1H NMR ($CDCl_3$, δ, ppm): 6.47 (s, 2H, Ar), 5.84 (m, 0.1H, $Ar-CH_2-CH=CH_2$), 4.99 (m, 0.2H, $Ar-CH_2-CH=CH_2$),

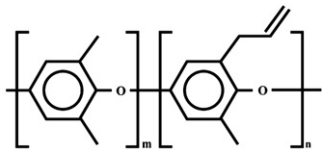

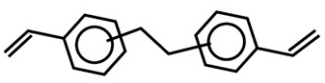

Scheme 1. Chemical structures of poly(2-allyl-6-methylphenol-*co*-2,6-dimethylphenol), (allyl-PPE), and bis(vinylphenyl) ethane, (BVPE).

3.21 (m, 0.2H, Ar–CH_2–CH=CH_2), and 2.09 (m, 5.7H, Ar–CH_3).

2.1.2. Synthesis of 1,2-bis(vinylphenyl) ethane (BVPE)

BVPE was prepared by the reported method [33]. A 500 ml three-necked flask equipped with nitrogen inlet tube, a 100-ml dropping funnel and a condenser was charged with magnesium turnings (4.02 g, 0.16 mol) and dry tetrahydrofuran (300 ml). The mixture was stirred and cooled to −5 °C. VBC (45.8 g, 0.30 mol) was added slowly into the mixture and the reaction system was stirred at 0 °C for 20 h. The reaction mixture was filtered and the solvent was evaporated. The residue was dissolved in 200 ml of hexane. The hexane solution was then washed with aqueous 1 M HCl once and with water twice, using a separatory funnel. The solution was dried over $MgSO_4$ and the solvent was evaporated. The product was dissolved in hexane and the solution was passed through a short column packed with silica gel. The purified product was obtained by removal of the solvent. BVPE was a mixture of *p*,*p*-isomer, *m*,*m*-isomer, and *m*,*p*-isomer (yield: 31.8 g, 91%).

IR (NaCl, ν, cm^{-1}): 906 cm^{-1} and 991 cm^{-1} (C=C). ^1H NMR ($CDCl_3$, δ, ppm): 7.00–7.35 (8H, multiplet, Ar), 6.69 (2H, Ar–CH=CH_2), 5.71, 5.21 (2H, Ar–CH=CH_2), 2.90 (4H, Ar–CH_2–CH_2–Ar).

2.2. Sample preparation

PPE and BVPE were dissolved in toluene to obtain 10 wt% solutions. Then, the solutions were dried to obtain plaques of the blends. Then, the plaques were cured at 230 °C under vacuum for 30, 45, 60 and 120 min. The compositions of the blends were 25/75, 50/50 and 75/25 (PPE/BVPE) in weight, which are denoted as N25, N50 and N75 for the blends with non-reactive PPE, respectively, and are denoted as R25, R50 and R75 for the blends with reactive allyl-PPE, respectively.

Thin sections of the samples with the thickness of about 60 nm were prepared by ultramicrotomy at room temperature and were collected on a 600-mesh copper grid. Then, the gold nanoparticles with diameter of 10 nm were dispersed on the specimens to be used as markers for focus adjustment and drift correction during the observation by dropping the aqueous Au colloid onto the specimens.

2.3. Energy-filtering transmission electron microscopy

An LEO922 in-column-type energy-filtering transmission electron microscope with a LaB_6 cathode equipped with an omega-type energy spectrometer was used at an accelerating voltage of 200 keV. The detailed instrumental setup was described in our previous papers [14,15]. Observations were carried out at room temperature or at −160 °C. To obtain high-resolution elemental maps and to perform quantitative chemical analysis, we employed image-EELS technique. Fig. 1 shows the scheme of the process employed in this work. First, a set of energy-filtered images were recorded sequentially across a wide range of energy loss to construct a 3-D data set containing spatial information, $I(x, y)$, and spectral information, $I(E)$. Then, the drift of the specimen during the acquisition was corrected by shifting the individual images pixel wise over the entire images acquired. The range of energy loss, the energy width for each image, and the energy increment between the neighboring images for oxygen were 450–600, 5, and 3 eV, respectively. Image-EELS enables us to acquire EELS spectra from areas of interest in any shapes in an image. EELS spectra from the regions of interest in an image can be synthesized by calculating the average gray values of the same pixels in each energy-filtered image over the whole range of acquired images. The image analysis system extracts intensities at the same pixel in each image across the series and reconstructs an EELS spectrum by plotting the intensities against the corresponding energy loss values. Thus, oxygen K-ionization edges (O K edge) originated from PPE can be obtained.

Oxygen elemental maps were created by "two-window jump ratio" method [26], selecting and using two recorded images among those acquired by image-EELS, where the energy-filtered image beyond the oxygen ionization edge at around 535 eV (post-edge image) was divided by the energy-filtered image below the ionization edge (pre-edge image). The energy position and the energy width of the two images used for the calculation of the elemental map should be determined to obtain an elemental map with a high S/N ratio. We optimized the quality of elemental maps by the following scheme: referring to the EELS spectra calculated by image-EELS. One proper pre-image for the BG fitting was selected from the stack

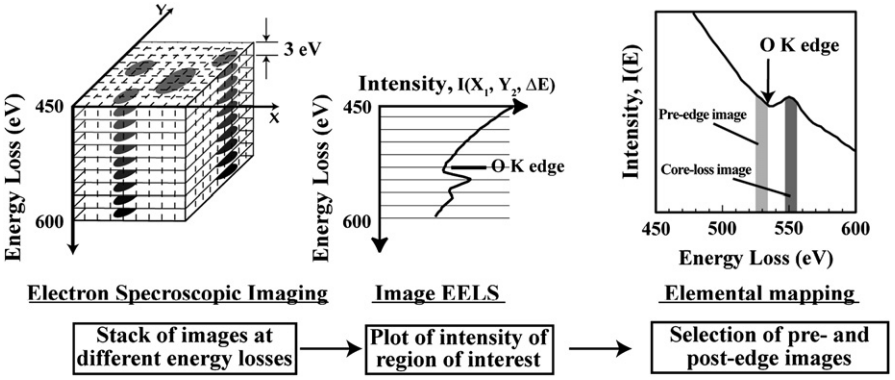

Fig. 1. Illustration representing the scheme of EFTEM analysis for high-resolution elemental mapping and quantitative EELS.

of images, and then the core-loss image was selected to give an elemental map with a high signal-to-noise ratio [16]. In this scheme, the energy width of each image for elemental mapping was adjusted by combining successive image into one image.

3. Results and discussion

3.1. Imaging and quantitative analysis of the phase separation of PPE/BVPE

The blends of PPE and BVPE are almost transparent even after the curing, which implies high miscibility between the two components or phase separation with sub-micrometer features with similar refractive indices of the two phases. It is thus difficult to find clouding points by optical microscopy in the curing process. BVPE has a similar molecular structure to styrene, which suggests high miscibility of the cured products like the blends of PPE and polystyrene. Fig. 2(a)–(c) shows energy-filtered images of N50 (PPE/BVPE 50/50) cured for 60 min, which are formed with the electrons without the energy losses (Fig. 2(a), zero-loss image), with inelastically scattered electrons with the energy losses of 525 ± 2.5 eV (Fig. 2(b), O K pre-edge image) and of 550 ± 2.5 eV (Fig. 2(c), O K core-loss image). Neither energy-filtered images nor conventional TEM images with a RuO_4 stained specimen showed any morphological features of the blend. On the other hand, an oxygen elemental map created by "two-window jump ratio" method using the pre-edge and the core-loss images, (Fig. 2(b) and (c), respectively), reveals the phase-separated morphology clearly owing to the difference in the oxygen concentrations between the two phases as shown in Fig. 2(d). The two phases are corresponding to the PPE-rich and the BVPE-rich phases, which are characterized as oxygen-rich and poor phases, respectively. Thus, the small differences in the compositions between the two phases can be identified by oxygen elemental mapping. Furthermore, we can estimate the differences of the oxygen concentrations between the two phases quantitatively by the process shown in Fig. 3. The borders between the two phases in the oxygen map are carefully determined as shown in Fig. 3(a), and then, EELS spectra including the oxygen K-edges are created from the two regions as shown in Fig. 3(b). The background intensities are subtracted from the spectra using the power law function [25], and then, the net signals originated from the ionization of oxygen can be obtained as shown in Fig. 3(c). Then, the integrated ratios of the two peaks with the energy width of 60 eV were calculated, which can be assigned to relative ratios of the two components.

3.2. Morphology development of PPE/BVPE via crosslinking reaction

The morphology developments of the blends in the curing process were investigated as shown in Fig. 4, where the

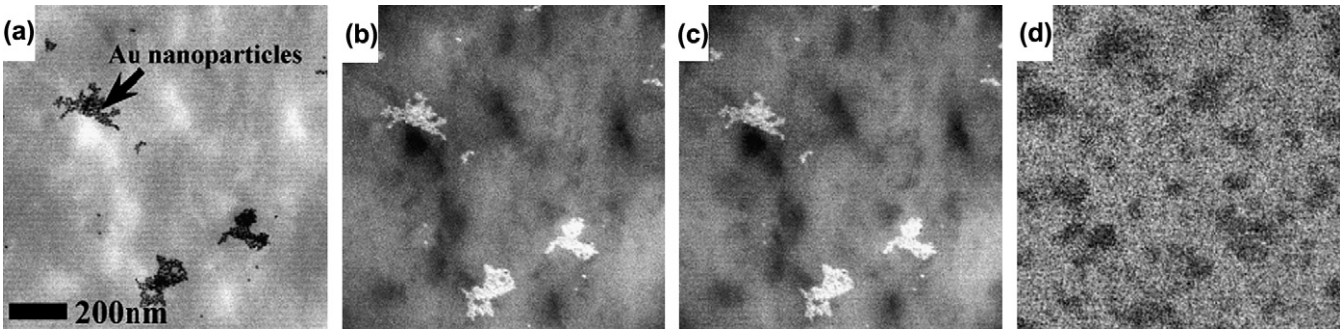

Fig. 2. A series of images of N50 showing (a) zero-loss image, (b) O K pre-edge image, (c) O K core-loss image and (d) oxygen map calculated by "two-window jump ratio" method in the same specimen position.

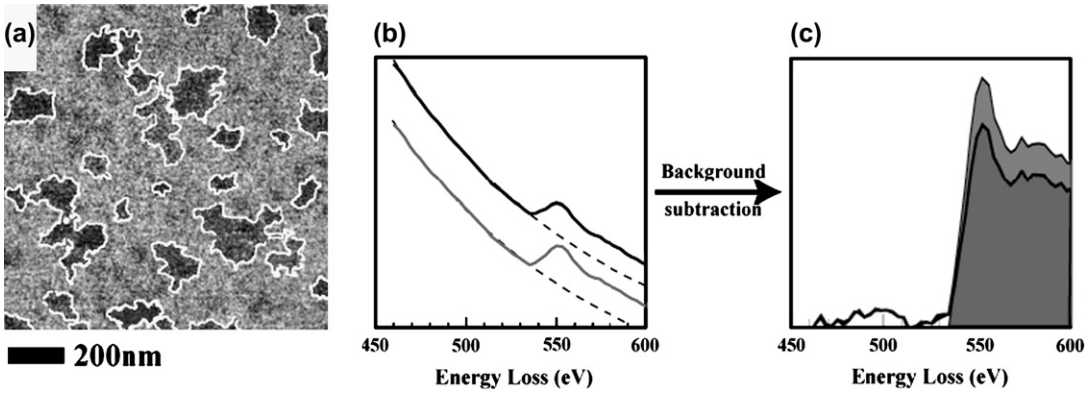

Fig. 3. Scheme for quantitative EELS analysis of the phase-separated morphologies of PPE/BVPE blends employed in this study: an oxygen map is separated into the oxygen-rich and poor regions (a), EELS spectra are created from the two regions (gray and black spectra are acquired from the oxygen-rich phase and the oxygen-poor phase, respectively) (b), and then the integrated areas under the oxygen core-loss peaks are calculated after the background subtraction (c).

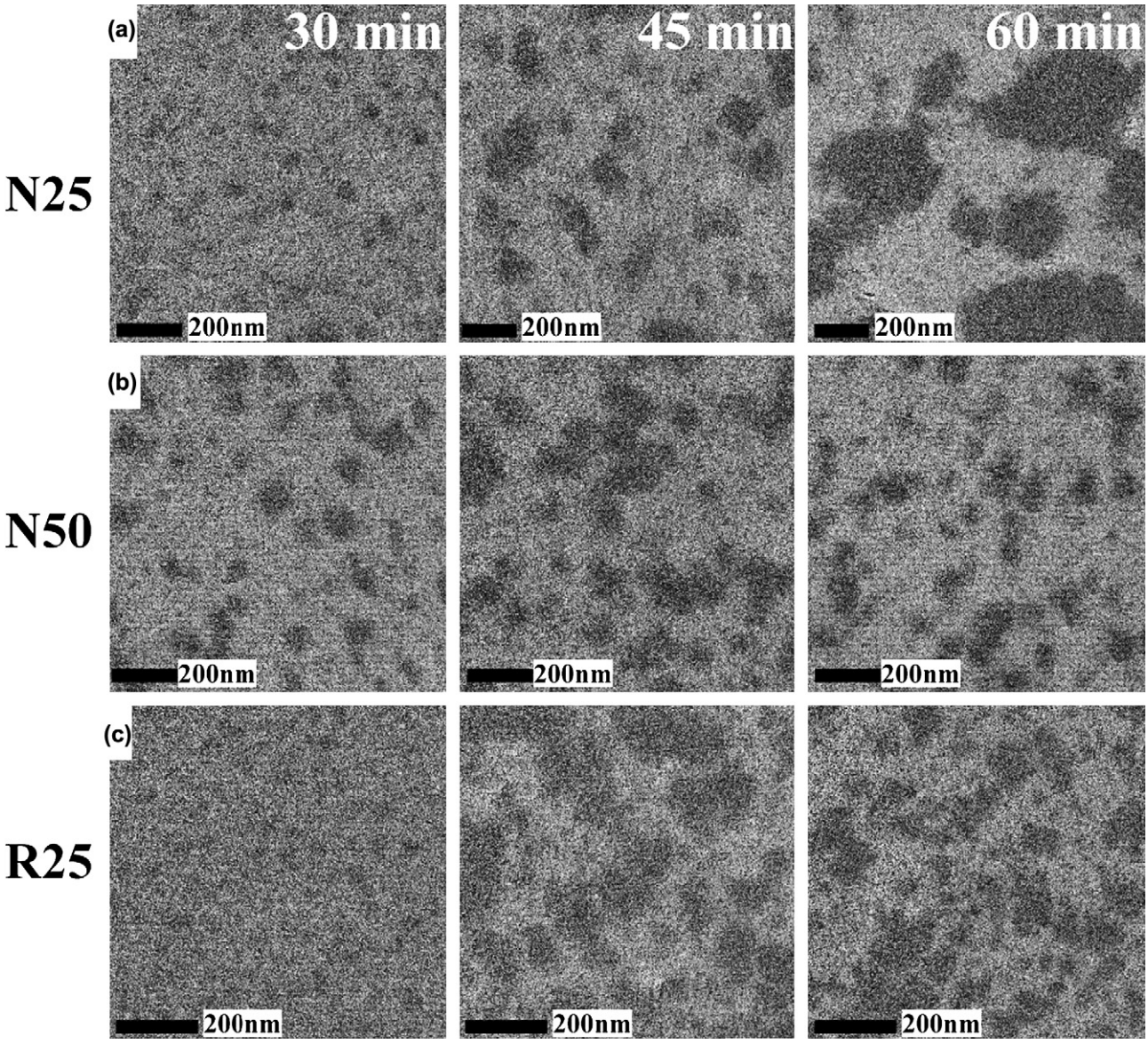

Fig. 4. Variation of oxygen maps with changes in the curing time and the composition of PPE/BVPE blends. The compositions of the blends are (a) N25, (b) N50 and (c) R25. Curing times are 30, 45 and 60 min for left, middle and right columns, respectively.

changes in the oxygen maps with increase of the curing time of N25 (BVPE-rich blend, Fig. 4(a), N50 (Fig. 4(b)) and R25 (Fig. 4(c)) with allyl-PPE containing 10 mol% of the reactive moiety (AMP) are shown. The samples were annealed at 230 °C for certain periods, and then those were dipped into liquid N_2 in order to freeze the developed phase-separated morphologies. All the observations were carried out at room temperature. The oxygen maps of N25 obviously indicate that the oxygen-poor domains (BVPE-rich phase) are produced in the PPE-rich matrix in the early stage of the curing and those are coarsened with increase of the curing time. The domain size of N50, on the other hand, seems to be kept in a similar level through the curing process, which is smaller than that in the BVPE-rich blend (N25). The growth of the BVPE-rich domains with increase of the curing time in R25 seems to be suppressed as compared to the blend with non-reactive PPE, indicating that the reaction between the two components suppresses the phase decomposition.

Effect of the reaction between PPE and BVPE on the phase decomposition was investigated by using allyl-PPEs having different reactive moiety contents. Fig. 5 shows the variation of the oxygen maps of allyl-PPE/BVPE blends of three different compositions (25/75, 50/50 and 75/25 in weight) with three different contents of the reactive moiety (5, 15 or 25 mol% of AMP unit is contained in PPE). The oxygen maps in the upper row of Fig. 5 are the blends with 25/75 (allyl-PPE/BVPE) composition, the middle row shows the maps of the blends of 50/50 composition, and the lower row shows the maps of the blends of 75/25 composition. AMP unit in allyl-PPE increases from left to right column in Fig. 5. The left, middle and right columns consist of the oxygen images of the blends with allyl-PPE having 5, 15 and

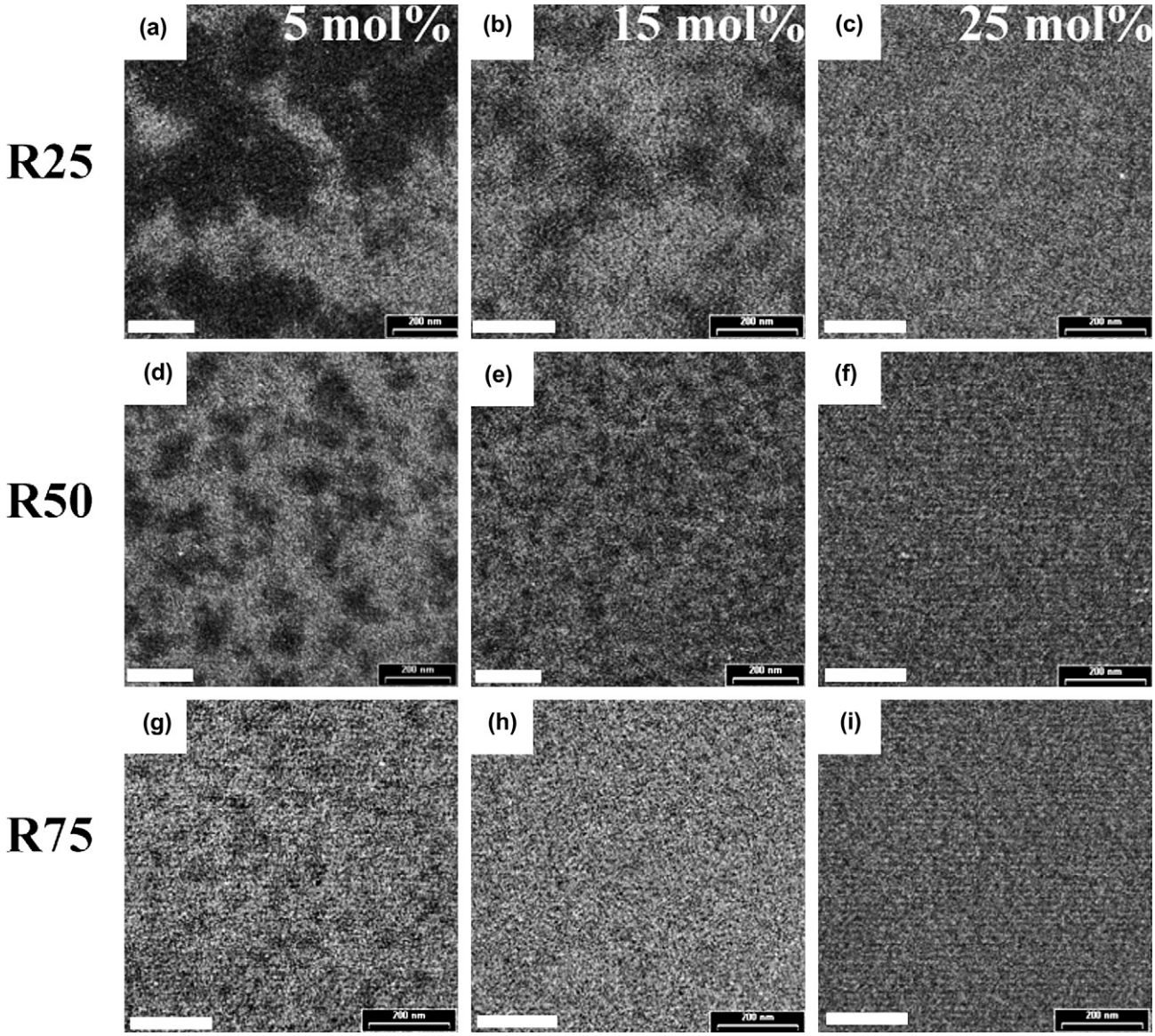

Fig. 5. Variation of oxygen maps of ally-PPE/BVPE blends by allyl-moieties in PPE. The compositions of the blends are (a–c) R25, (d–f) R50 and (g–i) R75. AMP fractions in PPE are (a, d and g) 5, (b, e and h) 15 and (c, f and i) 25 mol% All scale bars correspond to the length of 200 nm.

25 mol% of the AMP unit, respectively. The samples were cured at 230 °C for 60 min, and then were quenched in liquid N_2 in order to freeze the phase-separated morphologies. With increase of the content of the reactive moiety in PPE (from the left to the right column in Fig. 5), the BVPE-rich domains tend to be smaller, and finally the blends exhibit no phase separation. Fig. 5 also indicates that with increase of the PPE content in the blend (from the upper row to the lower in Fig. 5), the phase separation becomes unclear and finally the blends show single-phase structures.

The effect of the content of the reactive moiety in PPE can be quantitatively evaluated by EELS spectra. Fig. 6 shows the oxygen elemental ratios between the oxygen-rich and poor regions estimated from the integrated ratios of the oxygen core-loss peaks of the two regions in the oxygen maps as a function of the concentration of the AMP unit in PPE. The two blend compositions (R25 and R50) show similar tendency, where the compositions of the two phases are close to each other and finally the blends become homogeneous with increase of the reactive moiety. When the AMP content is 5 mol%, the phase-separated morphologies are similar to those of the non-reactive blends. On the other hand, when the AMP concentration increases to 10 mol%, the oxygen elemental ratios drastically decrease and then are kept in the similar levels, implying that 10 mol% of AMP is sufficient to suppress the phase decomposition of the blends by the reaction between PPE and BVPE.

3.3. Mechanisms of reaction-induced phase decomposition of PPE/BVPE system

We found that slow cooling of the samples leads to further developments of the phase decomposition. Fig. 7 shows the differences of the morphologies caused by cooling processes

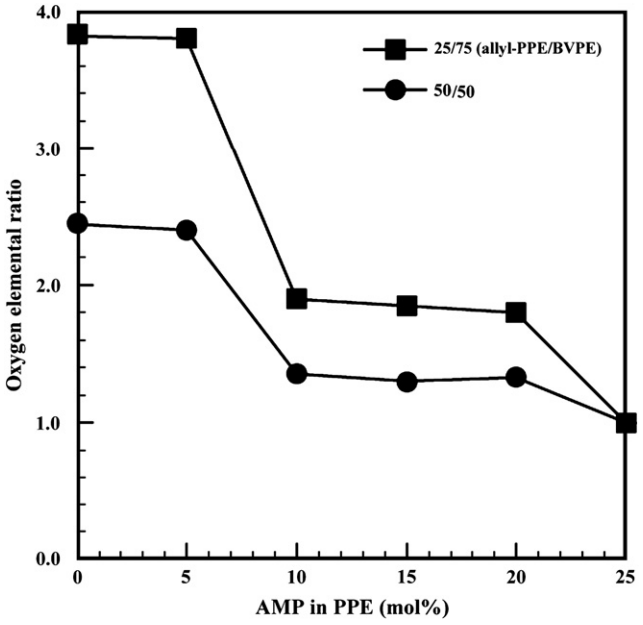

Fig. 6. Oxygen elemental ratios of the two phases in allyl-PPE/BVPE blends as a function of AMP fraction in PPE.

of the blends with non-reactive PPE (N25, N50 and N75) cured at 230 °C for 60 min. The upper row of Fig. 7 shows the maps of the samples quenched in liquid N_2, while the lower row shows those cooled from 230 °C to room temperature *in vacuo* approximately for 30 min. The oxygen-poor domains (BVPE-rich phase) are coarsened during the slow cooling process in N25 (Fig. 7(a) and (d) and N50 (Fig. 7(b) and (e)), while the phase decomposition of N75 initiates during the slow cooling process as shown in Fig. 7(c) and (f). The same tendency was shown also in the blends with reactive PPE (allyl-PPE with 10 mol% of AMP unit) as shown in Fig. 8. However, when introducing the reaction between PPE and BVPE, the composition range of the blends to show phase separation become narrower than those of the blends with non-reactive PPE. Only R25 shows the phase separation (Fig. 8(a)) when the samples quenched rapidly and R75 shows no phase-separated morphology even after the slow cooling (Fig. 8(f)).

The results suggest that the BVPE/PPE system has upper critical solution temperature (UCST) below the curing temperature (230 °C). The slow cooling process provides sufficient time to rearrange the polymer chains to form thermodynamically stable structures when the blends go into the two-phase region. Therefore, it is suggested that cooling process after cure is one of the important factors to determine the morphologies. In addition, the results indicate that the BVPE-rich blends show the distinct phase separations with relatively coarse domains, while the PPE-rich blends show fine dispersions with small compositional differences or single-phase features, suggesting that the PPE/BVPE blend system has asymmetric phase diagram in terms of the composition, having wider one-phase region in the BVPE-rich blends.

The phase-separated morphologies of the blends were characterized quantitatively using two parameters: oxygen elemental ratios between the two phases estimated from the EELS

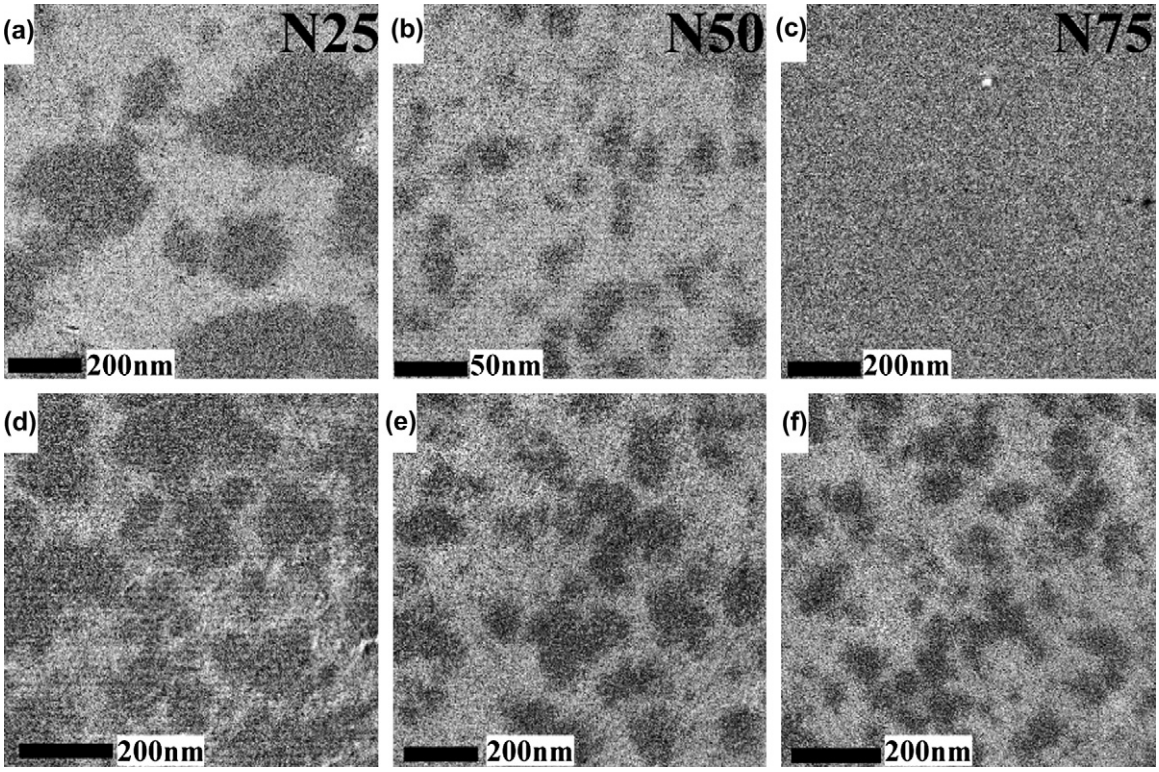

Fig. 7. Oxygen maps of N25 (a and d), N50 (b and e), N75 (c and f) cured for 60 min. Upper row shows the maps of the samples quenched in liquid N_2, while lower row shows the maps of the samples cooled slowly *in vacuo*.

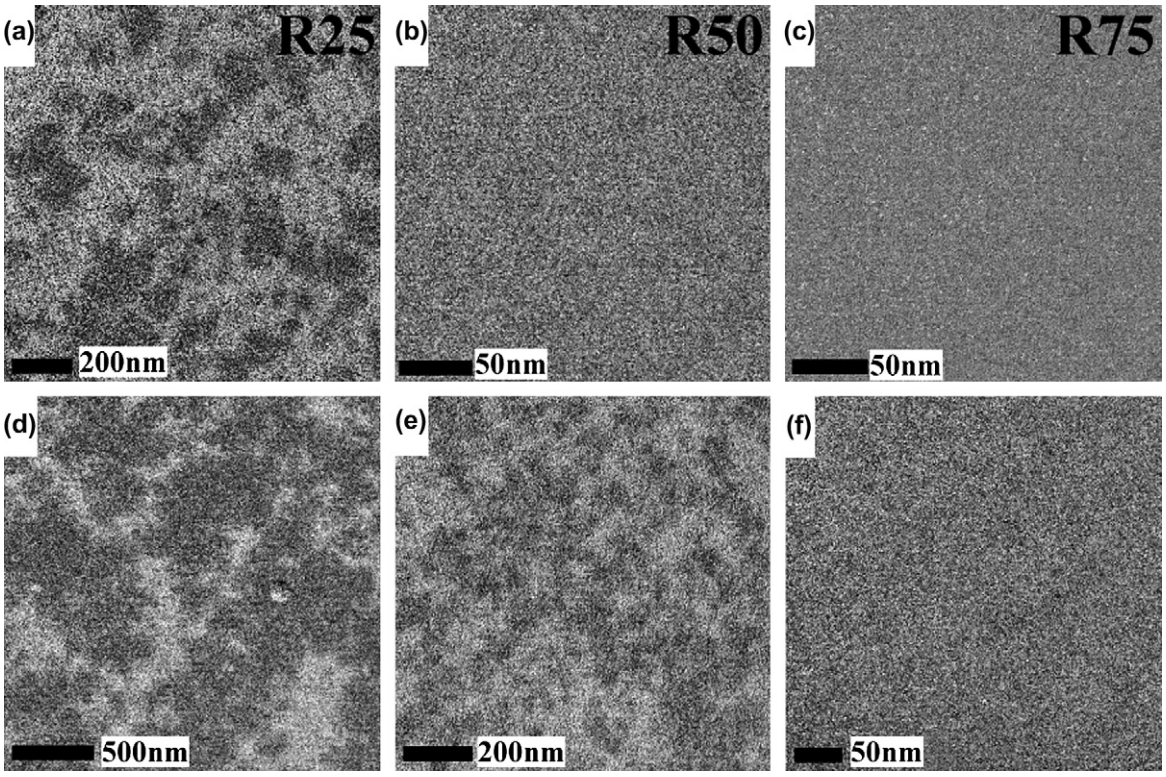

Fig. 8. Oxygen maps of R25 (a and d), R50 (b and e), R75 (c and f) cured for 60 min. AMP fraction in allyl-PPE is 10 mol%. Upper row shows the maps of the samples quenched in liquid N_2, while lower row shows the maps of the samples cooled slowly *in vacuo.*

spectra and the area fractions of the oxygen-rich phase estimated from the binarized oxygen maps, which are plotted as a function of the curing time in Fig. 9(a) and (b), respectively. N25 blend shows large increase in the ratios of the oxygen concentration between the two phases with increase of the curing time, while the other blends show only slight increase as shown in Fig. 9(a). The area fractions of the oxygen-rich phase, on the other hand, show slight decreases in all the evaluated blends, indicating that the phase separation proceeds during the curing process in all the blends. However, the ratios of the compositions of the two phases are kept in the similar levels at approximately 2 except for N25, suggesting that the

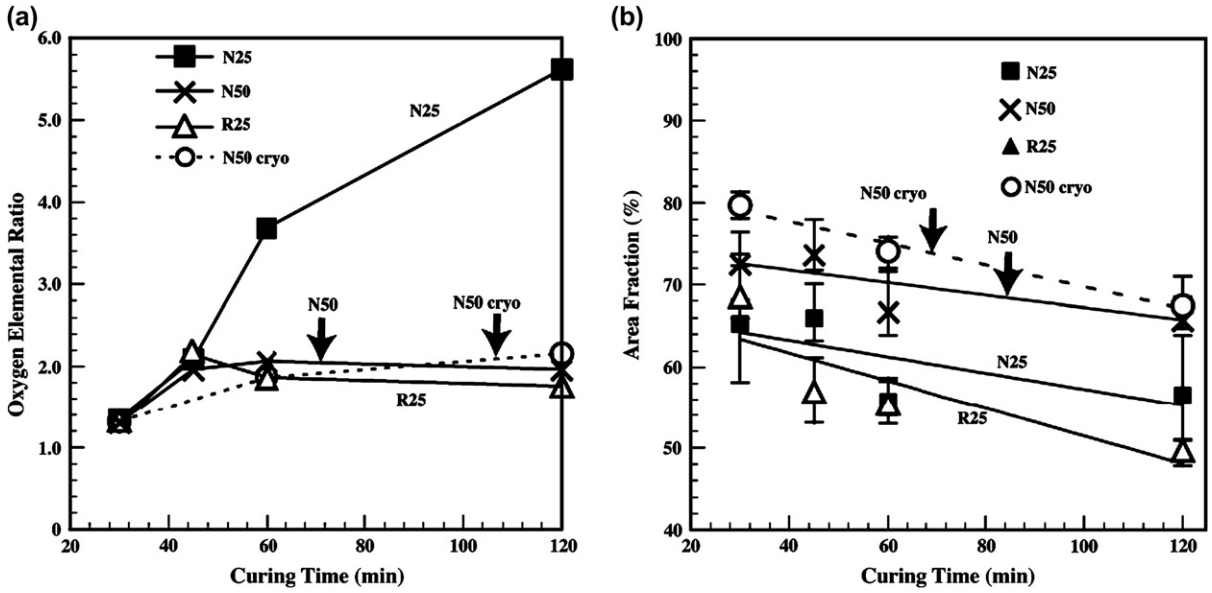

Fig. 9. (a) Oxygen elemental ratio between the two phases (ratio of PPE-rich phase to BVPE-rich phase) estimated from EELS spectra and (b) area fraction of oxygen-rich phase in PPE/BVPE blends of N25, N50 and R25 as a function of the curing time. The results obtained in the cryogenic condition of N50 are also plotted.

phase separation scheme of N25 is different from those of the other blends.

The effect of the radiation damage of the specimens during the observation by EFTEM should be considered for quantitative analysis of EELS. Damage of polymer specimens by electron beam cannot be avoided, which causes chain session and loss of mass during the irradiation of the electron beam. Therefore, the observation under cryogenic condition is recommended to minimize the radiation damage. The results obtained under a cryogenic condition at −160 °C of N50 are also plotted in Fig. 9, showing that no significant differences were achieved between the two observation conditions. Therefore, although the chemical structures of the polymers are changed by the electron beam during the TEM observation, the elemental compositions may not be significantly changed, which allows us the quantitative analysis of the phase decomposition processes at room temperature.

Reaction-induced phase decomposition has been interpreted as changes in a phase diagram with increase in the molecular weight of components [34]. Spinodal and binodal curves move as the molecular weight increases so that the two-phase region prevails in a phase diagram. A mixture that is initially in a single-phase system is thrust into a two-phase regime as the curing reaction proceeds so that phase decomposition takes place. If the system is thrust into the meta-stable region between the spinodal and binodal lines, the phase decomposition proceeds by nucleation and growth mechanism (N&G). In the N&G scheme, isolated particles with an equilibrium composition initially appear and then grow up to produce an irregular two-phase structure in which one phase is dispersed within the other continuous matrix. If the system is thrust into the unstable region under the spinodal line, spinodal decomposition (SD) takes place, in which the phase decomposition starts with the concentration fluctuation, and then it attains a two-phase structure with two equilibrium compositions.

Therefore, the phase decomposition scheme of the PPE/BVPE blend system induced by the crosslinking reaction can be understood as the shift of the phase diagram as illustrated in Fig. 10. The UCST-type phase boundary of the blends before the curing is located below the curing temperature. The boundary is elevated as the polymerization of BVPE proceeds. The 25/75 PPE/BVPE non-reactive blend is thrust into the unstable region under the spinodal line to induce the phase decomposition by SD. On the other hand, the 50/50 PPE/BVPE blend may be in the meta-stable region between the binodal and spinodal lines, which means that the quench depth is lower than N25, so that the phase decomposition proceeds by N&G. The 75/25 PPE/BVPE blend shows no phase separation even after the curing, indicating that this composition stays in the one-phase region even after the curing. However, this blend composition will pass the UCST during the cooling process, and thus the phase decomposition occurs. In the allyl-PPE/BVPE blends, only the 25/75 blend shows the two-phase structure which may be developed by N&G. Therefore, the one-phase/two-phase boundary after curing is located between 25/75 and 50/50 compositions. This means that the reaction between PPE and BVPE shifts the UCST curve toward the lower PPE fraction side.

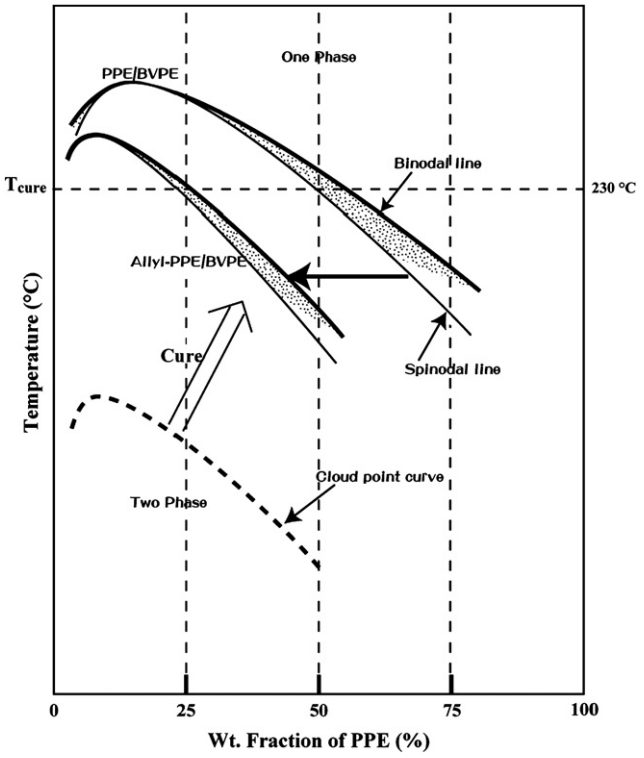

Fig. 10. Schematic representation of the shifts of the phase diagram of PPE/BVPE blend system induced by the curing reactions.

4. Conclusions

EFTEM enables to characterize the phase-separated morphologies of the PPE/BVPE blends, which cannot be observed by conventional TEM. The oxygen mapping can visualize small differences of the oxygen concentration in the blends, which allows us to see the phase separation describing as oxygen-rich (PPE-rich) and poor (BVPE-rich) regions. Moreover, the morphologies can be quantitatively characterized by EELS, which allows us to investigate the phase decomposition processes induced by the crosslinking reactions. We show the advanced application and possibility of EFTEM for the investigation of polymer structures. In this study, the observation performed in room temperature and in cryogenic condition gave no significant differences in the results. It is important to be able to perform the analysis without the time-consuming cryogenic observation. The samples investigated in this study contain large amount of aromatic moieties and crosslinks that may give high resistivity against the electron beam.

Acknowledgement

Financial support by NEDO ‘‘Nanostructured Polymer Project’’ is greatly appreciated.

References

[1] Goossens S, Goderis B, Groeninckx G. Macromolecules 2006; 39(8):2953–63.
[2] Buxton GA, Clarke N. Macromolecules 2005;38(21):8929–38.
[3] Nephew JB, Nihei TC, Carter SA. Phys Rev Lett 1998;80(15): 3276–9.
[4] Tran-Cong Q, Harada A. Phys Rev Lett 1996;76(7):1162–5.
[5] Furukawa H. J Phys Soc Jpn 1994;63(10):3744–50.
[6] Harada A, Tran-Cong Q. Macromolecules 1997;30(6):1643–50.
[7] Kimura K, Inoue H, Kohama SI, Yamashita Y, Sakaguchi Y. Macromolecules 2003;36(20):7721–9.
[8] Girard-Reydet E, Pascault JP. Macromolecules 2000;33(8):3084–91.
[9] Li W, Ryan AJ, Meier IK. Macromolecules 2002;35(13):5034–42.
[10] Rebizant V, Venet AS, Tournilhac F, Girard-Reydet E, Navarro C, Pascault JP, et al. Macromolecules 2004;37(21):8017–27.
[11] Swier S, Van Mele B. Macromolecules 2003;36(12):4424–35.
[12] Varlot K, Martin JM, Quet C. Polymer 2000;41(12):4599–605.
[13] Du Chesne A. Macromol Chem Phys 1999;200(8):1813–30.
[14] Horiuchi S, Hamanaka T, Aoki T, Miyakawa T, Narita R, Wakabayashi H. J Electron Microsc 2003;52(3):255–66.
[15] Horiuchi S, Yin D, Ougizawa T. Macromol Chem Phys 2005; 206(7):725–31.
[16] Hofer F, Warbichler P, Grogger W. Ultramicroscopy 1995;59(1–4): 15–31.
[17] Shimizu T, Iwaura R, Masuda M, Hanada T, Yase K. J Am Chem Soc 2001;123(25):5947–55.
[18] Nakazawa I, Masuda M, Okada Y, Hanada T, Yase K, Asai M, et al. Langmuir 1999;15(14):4757–64.
[19] Masuda M, Hanada T, Okada Y, Yase K, Shimizu T. Macromolecules 2000;33(25):9233–8.
[20] Rom I, Hofer F, Bucher E, Sitte W, Gatterer K, Fritzer HP, et al. Chem Mater 2002;14(1):135–43.
[21] Correa CA, Hage E. Polymer 1999;40(8):2171–3.
[22] Horiuchi S, Hanada T, Yase K, Ougizawa T. Macromolecules 1999;32(4):1312–4.
[23] Horiuchi S, Ishii Y. Polym J 2000;32(4):339–47.
[24] Horiuchi S, Fujita T, Hayakawa T, Nakao Y. Langmuir 2003;19(7): 2963–73.
[25] Horiuchi S, Dohi H. Langmuir 2006;22(10):4607–13.
[26] Wang ZL. Characterization of nanophase materials. Weinheim, Germany: Wiley-VCH; 2000. p. 37–80.
[27] Costa CAR, Leite CAP, de Souza EF, Galembeck F. Langmuir 2001;17(1):189–94.
[28] Amou S, Yamada S, Nagai A, Miwa T, Tomoi M. Kobunshi Ronbunshu 2004;61(9):474–82.
[29] Ishii Y, Ryan AJ. Macromolecules 2000;33(1):158–66.
[30] Venderbosch RW, Meijer HEH, Lemstra PJ. Polymer 1994;35(20):4349–57.
[31] Nunoshige J, Shibasaki Y, Ueda M. Chem Lett 2007;36(2):238–9.
[32] Fukuhara T, Shibasaki Y, Ando S, Ueda M. Polymer 2004;45(3):843–7.
[33] Amou S, Yamada S, Takayanagi A, Nagai A, Miwa T, Tomoi M. J Appl Polym Sci 2004;92(2):1252–8.
[34] Inoue T. Prog Polym Sci 1995;20(1):119–53.